

## CERAMICS

## Borrowed dislocations for ductility in ceramics

L. R. Dong<sup>1,2,3†</sup>, J. Zhang<sup>2†</sup>, Y. Z. Li<sup>3†</sup>, Y. X. Gao<sup>4</sup>, M. Wang<sup>3</sup>, M. X. Huang<sup>3\*</sup>,  
J. S. Wang<sup>1\*</sup>, K. X. Chen<sup>4\*</sup>

The inherent brittleness of ceramics, primarily due to restricted atomic motions from rigid ionic or covalent bonded structures, is a persistent challenge. This characteristic hinders dislocation nucleation in ceramics, thereby impeding the enhancement of plasticity through a dislocation-engineering strategy commonly used in metals. Finding a strategy that continuously generates dislocations within ceramics may enhance plasticity. Here, we propose a “borrowing-dislocations” strategy that uses a tailored interfacial structure with well-ordered bonds. Such an approach enables ceramics to have greatly improved tensile ductility by mobilizing a considerable number of dislocations in ceramic borrowed from metal through the interface, thereby overcoming the challenge associated with direct dislocation nucleation within ceramics. This strategy provides a way to enhance tensile ductility in ceramics.

Ceramics exhibit attractive properties for a range of applications, including high hardness, high strength, excellent corrosion resistance, and a notable tolerance to high temperatures. These properties make ceramics useful across diverse fields such as aerospace and automotive engineering, energy storage, electronics, and semiconductors (1–8). However, ceramics are intrinsically brittle at ambient temperatures because of strong chemical bonds, which lead to a high threshold stress required for dislocation nucleation and impede the initiation of dislocations (9–14). Preinducing a substantial density of dislocations is feasible under extreme conditions (14, 15); this can achieve a dislocation density on the order of  $10^{15} \text{ m}^{-2}$  and effectively enhances ceramic toughness. However, once these preinduced dislocations have been exhausted, nucleating new dislocations for continuous deformation is difficult, thus triggering rupture of the chemical bonds and eventual catastrophic failures. Therefore, the high threshold stress for dislocation nucleation in ceramics substantially limits the potential for improving plasticity through a dislocation-engineering strategy (16–18). As a result, several strategies have been directed toward achieving better plasticity in ceramics through alternative mechanisms (8, 9, 19–23). In our previous work, for instance, we improved the compressive plasticity of silicon nitride ceramic through bond switching at coherent interfaces (20). Nonetheless, achieving tensile ductility in ceramics presents a more formidable challenge, pri-

marily because of the difficulty of dislocation nucleation under tensile loads, where even minute defects can trigger premature crack-ing prior to dislocation initiation.

To endow ceramics with tensile ductility, one avenue worth exploring involves inducing a continuous generation of dislocations within these materials. For this purpose, we propose a “borrowing-dislocations” strategy. This strategy entails continuously borrowing externally nucleated dislocations from metals and introducing them into ceramics, with the aim of bypassing the difficulty of direct nucleation of dislocations within ceramics. In this way, the critical stress required for motion of borrowed dislocations is markedly lower than the theoretical threshold for nucleation of dislocation in ceramics, thus facilitating a more facile route for continuous propagation and multiplication of dislocations in ceramics.

To implement our borrowing-dislocations strategy, it was necessary to establish a dedicated transfer channel for metal-ceramic dislocations. A chemically orderly-bonded metal-ceramic interface (which we call an orderly-bonded interface) is required to tolerate the large stress induced by the borrowed dislocations. Additionally, ensuring the continuity and alignment of crystallographic planes between metal and ceramic is crucial to minimize the energy barrier associated with dislocation slip across the interface. Meanwhile, this alignment helps alleviate stress concentration due to the dislocation accumulation at the interface. Guided by these two criteria, we tailored orderly-bonded interfaces aimed at building the dislocation transfer channel between metals and ceramics, emphasizing more than just establishing the interface by comparing lattice symmetries and parameters. We identified a lanthanum oxide ( $\text{La}_2\text{O}_3$ ) ceramic as one material capable of forming such an orderly-bonded interface with a molybdenum (Mo) metal. We conducted density functional theory (DFT) calculations to elucidate the high coherency and strong chem-

ical bonds at this interface (fig. S1). Our DFT results reveal a substantial increase in adhesion energy (or separation energy) at the orderly-bonded interfaces between the  $\text{La}_2\text{O}_3$  ceramic and Mo metal, exceeding that of the disorderly-bonded interfaces (fig. S2 and table S1). This enhanced adhesion energy holds promise for enhancing the slip transfer process of the borrowed dislocations, positioning the  $\text{La}_2\text{O}_3$ -Mo system as a promising candidate for validating our borrowing-dislocations strategy. Therefore, we prepared the dislocation-borrowing  $\text{La}_2\text{O}_3$  ceramic (DB  $\text{La}_2\text{O}_3$ ) to demonstrate this strategy by tailoring an orderly-bonded  $\text{La}_2\text{O}_3$ -Mo heterointerfacial structure.

We derived inspiration from the sophisticated epitaxial structure commonly used in two-dimensional semiconductor films (24–26) and adopted this epitaxial-growth philosophy to tailor our desire for an orderly-bonded interface within three-dimensional (3D) bulk materials. The key to crafting this interface lies in selecting one substance as the substrate while inducing the recrystallization of another substance on this substrate. Specifically, the DB  $\text{La}_2\text{O}_3$  ceramic grown epitaxially with the Mo metal was fabricated by a carefully designed high-temperature, long-duration sintering process aimed at facilitating the epitaxial growth between the  $\text{La}_2\text{O}_3$  ceramic and Mo metal (27). As a result, the tailored metal-ceramic interfaces we observed in the polycrystalline DB  $\text{La}_2\text{O}_3$  sample exhibit minimal misorientations, with boundary angles measuring  $<2^\circ$ , which provides indication of a high degree of coherency in the arrangement between the  $\text{La}_2\text{O}_3$  ceramic and Mo metal (fig. S3, A and B). In contrast, the metal-ceramic interfaces in the reference  $\text{La}_2\text{O}_3$ -Mo sample without the tailored interface exhibit boundary misorientations of up to  $90^\circ$  (fig. S3, C and D).

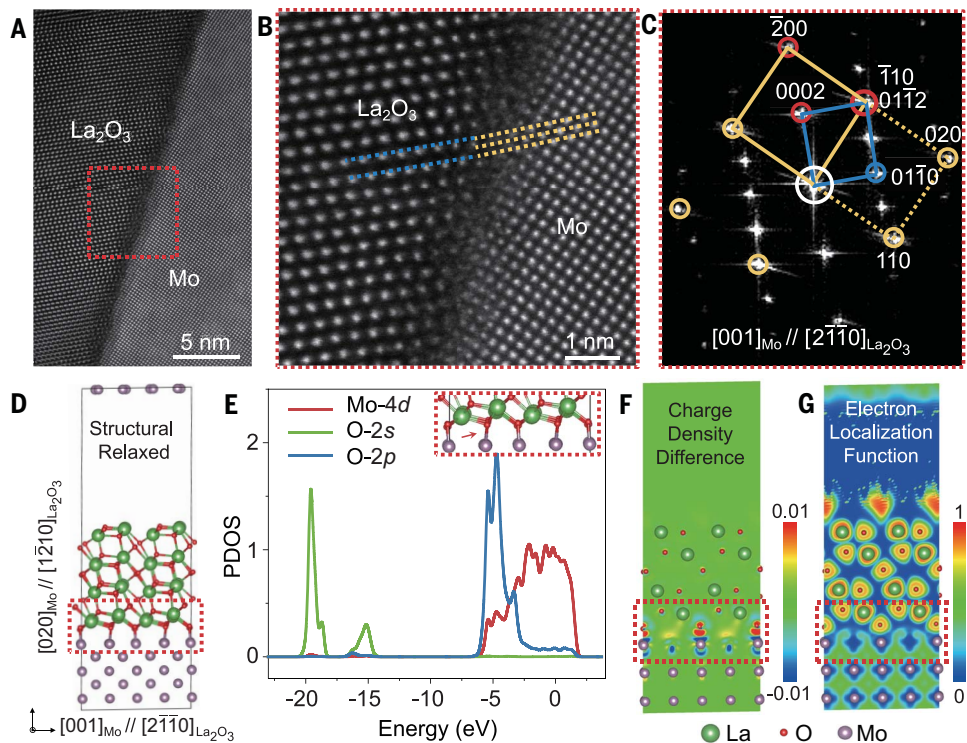
We performed high-angle annular dark-field scanning transmission electron microscopy (HAADF-STEM) analysis to directly characterize the tailored metal-ceramic interface. The results demonstrate that the DB  $\text{La}_2\text{O}_3$  sample exhibits a highly coordinative arrangement at the metal-ceramic interface, showcasing orderly-bonded coherent or semicoherent interfaces with various matched relationships (Fig. 1, A to C, and fig. S4), consistent with our DFT results (fig. S1). Meanwhile, our results confirm the capability of hexagonally structured  $\text{La}_2\text{O}_3$  and body-centered cubic Mo to sustain orderly-bonded interfaces despite the presence of lattice mismatch. Notably, we identified an orderly-bonded interface, where the (0002) planes of  $\text{La}_2\text{O}_3$  are parallel to the (200) planes of Mo with  $2d_{\text{Mo}(200)}$  equal to  $d_{\text{La}_2\text{O}_3(0002)}$  and a low misfit of 2.06%, meanwhile the (0112) planes of  $\text{La}_2\text{O}_3$  are parallel to the (110) planes of Mo with  $d_{\text{Mo}(110)}$  equal to  $d_{\text{La}_2\text{O}_3(0112)}$  and a low misfit of 2.46%. Theoretically, such atomic-scale orderly-bonded

<sup>1</sup>MOE Key Laboratory of Advanced Functional Materials, College of Materials Science and Engineering, Beijing University of Technology, Chaoyang District, Beijing 100124, China. <sup>2</sup>Advanced Structural Ceramics Innovation Center, Yongjiang Laboratory, Ningbo 315202, China. <sup>3</sup>Department of Mechanical Engineering, The University of Hong Kong, Pokfulam Road, Hong Kong 999077, China. <sup>4</sup>State Key Laboratory for Advanced Metals and Materials, University of Science and Technology Beijing, Beijing 100083, China.

\*Corresponding author. Email: kxchen@ustb.edu.cn (K.X.C.); wangjs@bjut.edu.cn (J.S.W.); mxhuang@hku.hk (M.X.H.)

†These authors contributed equally to this work.

**Fig. 1. Microstructure and chemical bonding calculation of DB  $\text{La}_2\text{O}_3$ .** (A to C) Atomic structure of a specific orderly-bonded interface in the DB  $\text{La}_2\text{O}_3$  sample characterized by HAADF-STEM, viewed along  $[001]_{\text{Mo}}$  and  $[2\bar{1}\bar{1}0]_{\text{La}_2\text{O}_3}$  directions, indicating excellent atomic-scale matching between  $(0002)_{\text{La}_2\text{O}_3}$  and  $(200)_{\text{Mo}}$  planes at the interface. (B) The magnified view of the red dashed box in (A). Specifically, the  $(0002)$  planes of  $\text{La}_2\text{O}_3$  are shown by blue dashed lines, and the  $(200)$  planes of Mo are shown by yellow dashed lines. The results indicate that the spacing of  $(0002)$  planes in  $\text{La}_2\text{O}_3$  is twice that of  $(200)$  planes in Mo. (C) The corresponding FFT pattern of the red dashed box in (A). The diffraction spot spacing of the  $(200)$  planes in Mo is twice that of  $(0002)$  planes in  $\text{La}_2\text{O}_3$ , which is consistent with the results illustrated in (B). (D to G) DFT calculation results on atomic and electronic structures of the ordered  $\text{La}_2\text{O}_3$ -Mo interface. (D) The relaxed interface model constructed on the basis of the atomic structure observed by TEM in (A) to (C). (E) PDOS of Mo and O atoms at the interface. There are several hybridization peaks between O-2s and Mo-4d in the range of  $-20.5$  to  $-18.5$  eV and between O-2p and Mo-4d in the range of  $-6.5$  to  $2.0$  eV, demonstrating strong chemical bonds between them. (F) Charge density difference map for the interface. The result indicates a strong charge transfer between the interfacial Mo and O. (G) ELF map for the interface, with the red (blue) contour suggesting the strong localization (delocalization) region of electrons. The electron localization between Mo and O atoms indicates strong Mo-O bonds with a mixed covalent and ionic character.



interfaces are deemed thermodynamically favorable during epitaxial growth owing to the minimization of interfacial energy (28). Meanwhile, the DFT simulation on the structure (Fig. 1D) was constructed on the basis of the above experimental observations, providing insights into the partial density of state (PDOS) (Fig. 1E), charge density difference (Fig. 1F), and electron localization function (ELF) (Fig. 1G) of the interfacial Mo, La, and O atoms. Notably, the PDOS results exhibit several hybridization peaks between O-2s and Mo-4d (in the range of  $-20.5$  to  $-18.5$  eV) and between O-2p and Mo-4d (in the range of  $-6.5$  to  $2.0$  eV), demonstrating strong chemical bonds between them. Furthermore, the results of charge density difference reveal a strong charge transfer at the interface between Mo and O atoms, with Mo atoms acting as electron donors and O atoms acting as electron acceptors. Specifically, the electrons accumulate in the region between Mo and O atoms and are shared by them, which is indicative of a typical covalent nature. Additionally, the Mo-O interaction exhibits an ionic nature owing to the charge polarization toward O. As such, the Mo-O bond demonstrates a hybrid combining covalent and ionic features. The ELF map illustrates strong electron localization between Mo and O atoms, reaffirming robust Mo-O bonds with a mixed covalent and

ionic character. This may substantially contribute to strengthening the interfaces and thereby facilitate our borrowing-dislocations strategy (29, 30).

To substantiate the impact of orderly-bonded interfacial structure on enhancing tensile ductility in ceramics, we evaluated the mechanical properties of the DB  $\text{La}_2\text{O}_3$  sample under TEM (Fig. 2 and fig. S5). The results show that the DB  $\text{La}_2\text{O}_3$  sample exhibits exceptional tensile ductility at room temperature, with a maximum tensile elongation exceeding 39.9% (Fig. 2A), manifesting the substantial tensile deformation capability of this ceramic. We conducted in situ tensile tests on larger micro-sized DB  $\text{La}_2\text{O}_3$  ceramics (longitudinal sizes ranging from  $5.3$  to  $20.5$   $\mu\text{m}$ ) at room temperature (fig. S6), revealing substantial tensile elongation (24.6 to 34.3%) in all specimens.

Furthermore, we captured more detailed deformation behavior of the ductile DB  $\text{La}_2\text{O}_3$  ceramic under tensile loading (Fig. 2B, fig. S7, and movies S1 and S2) and compared it to that of the normal  $\text{La}_2\text{O}_3$  ceramic (Fig. 2C and movie S3). A crucial observation revealed that the ductile DB  $\text{La}_2\text{O}_3$  ceramic showed exceptional resistance to catastrophic fracture. This behavior was markedly different from that of the normal  $\text{La}_2\text{O}_3$  ceramic, where crack initiation occurred at a strain of 1.7% and then

rapidly propagated toward the interface, culminating in fracture failure at a strain of 1.8% (Fig. 2C). This comparison confirms that the intrinsic brittleness of the  $\text{La}_2\text{O}_3$  ceramic was overcome by our borrowing-dislocations strategy. Despite the combined effect of the electron beam irradiation and the sample size, the normal  $\text{La}_2\text{O}_3$  ceramic displayed a higher elastic deformation, along with the typical tensile stress-strain curve previously depicted in ceramics without structural mediation (20). However, fracture failure of the normal  $\text{La}_2\text{O}_3$  ceramic occurred rapidly without any plastic deformation, thus leading to negligible tensile plasticity. In contrast, the DB  $\text{La}_2\text{O}_3$  ceramic with the tailored interface demonstrated not only an elastic modulus comparable to that of the normal  $\text{La}_2\text{O}_3$  ceramic but also an exceptional tensile plasticity more similar to the behavior of metals.

More specifically, we found that the DB  $\text{La}_2\text{O}_3$  sample underwent further plastic deformation in a serrated manner, with the peak stress of these serrations decreasing as deformation progressed (Fig. 2A). The strain burst, known as a shear avalanche, triggered a sudden drop in stress, followed by repetitive cycles of elastic reloading and shear avalanches, typically corresponding to the nucleation-multiplication-accumulation-slip processes of dislocations



in the substance during plastic deformation (31, 32). Generally, the slopes of the elastic reloading curves remain consistent owing to the deformation coherency of the homogeneous substance (31, 33). However, we found a dis-

cernible difference in slope among the curve of the current DB  $\text{La}_2\text{O}_3$  sample, implying the movement of dislocations in different substances. Additionally, the in situ tensile observation (movies S1, S2, and S4) revealed an

abnormal dislocation multiplication in the DB  $\text{La}_2\text{O}_3$  ceramic during plastic deformation, potentially contributing to the metal-like ductility observed in the ductile DB  $\text{La}_2\text{O}_3$  ceramic.

To elucidate the dislocation characteristics in the ductile DB  $\text{La}_2\text{O}_3$  ceramic, we performed **g·b** analysis on the DB  $\text{La}_2\text{O}_3$  sample strained to 12% by TEM (Fig. 3, A to D), where **g** is the diffraction vector and **b** is the Burgers vector. Abundant dislocation segments in the DB  $\text{La}_2\text{O}_3$  ceramic were visible under **g** = 0002 and **g** =  $\bar{2}110$  two-beam conditions. This observation, along with the bright-field TEM images with varied deviation parameters (fig. S8), confirms that the visible dislocation segments are  $\langle c + a \rangle$  dislocations. Some dislocations that were invisible under **g** = 0002 were visible under **g** =  $\bar{2}110$ , indicating they are  $\langle a \rangle$  dislocations. In addition, a few dislocations invisible under **g** =  $\bar{2}110$  but visible under **g** = 0002 were identified to be  $\langle c \rangle$  dislocations.

In addition, we calculated the densities of  $\langle a \rangle$ ,  $\langle c \rangle$ , and  $\langle c + a \rangle$  dislocations within the DB  $\text{La}_2\text{O}_3$  samples at different tensile strains by neutron diffraction (Fig. 3, E and F, and figs. S9 to S12). The results (Fig. 3F) reveal that both  $\langle c + a \rangle$  and  $\langle a \rangle$  dislocation densities continuously increase with increasing tensile strain, with  $\langle c + a \rangle$  dislocations multiplying at a faster rate than  $\langle a \rangle$  dislocations. The density of  $\langle c \rangle$  dislocations remains unchanged, aligning with their sessile nature. As is known,  $\langle a \rangle$  dislocations only glide on basal or prismatic

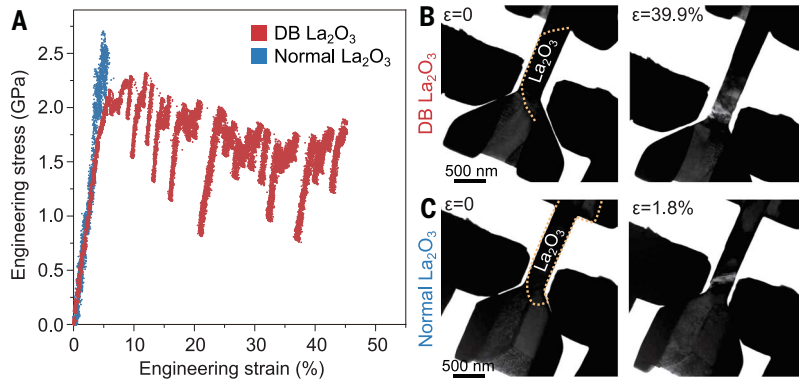
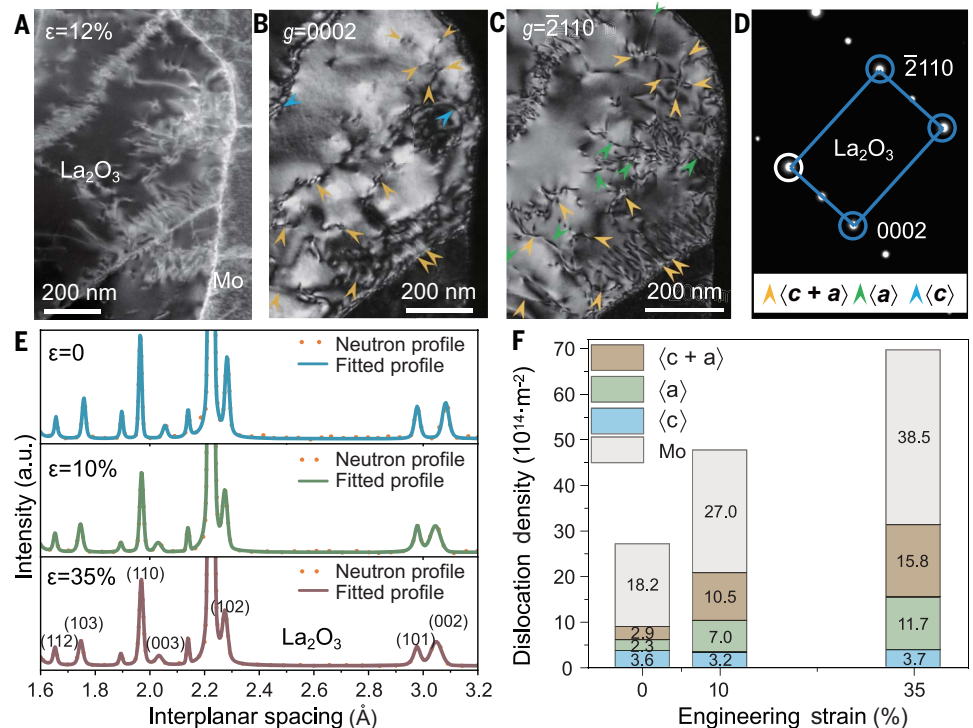


**Fig. 2. Room temperature in situ tensile test under TEM.** (A) The engineering stress-strain curves acquired during the tensile deformation of sheetlike DB  $\text{La}_2\text{O}_3$  and normal  $\text{La}_2\text{O}_3$  samples with dimensions of 1200 nm by 410 nm by 135 nm and 1500 nm by 330 nm by 120 nm, respectively. The tensile strain rate is  $2 \times 10^{-3} \text{ s}^{-1}$ . The diffraction patterns of these ceramics are shown in fig. S5. The results illustrate the success of our borrowing-dislocations strategy in imparting metal-like tensile ductility to the intrinsically brittle normal  $\text{La}_2\text{O}_3$  ceramics through the orderly-bonded interfacial mediation. (B and C) Snapshots from real-time movies of in situ tensile test of the samples at strains ( $\epsilon$ ) of 0 and 39.9% (DB  $\text{La}_2\text{O}_3$ ; movie S1) and 0.0 and 1.8% (normal  $\text{La}_2\text{O}_3$ ; movie S3), respectively. The yellow dotted curves indicate the shape of the  $\text{La}_2\text{O}_3$  ceramics. The results of (B) and (C) reveal that the DB  $\text{La}_2\text{O}_3$  sample after interfacial mediation exhibits high resistance to interface debonding and ceramic fracture even after undergoing substantial deformation under tensile loading. The fracture mode of the DB  $\text{La}_2\text{O}_3$  sample differs from that of the normal  $\text{La}_2\text{O}_3$  ceramic, which typically undergoes brittle fracture.

**Fig. 3. Dislocation behavior in the ceramics.**

(A to D) Dislocations in a DB  $\text{La}_2\text{O}_3$  ceramic after tensile straining to 12%. (A) The bright-field STEM image. (B) The dark-field and (C) bright-field TEM observations of the same region in (A) that were conducted under a two-beam condition. Abundant  $\langle c + a \rangle$  dislocation segments (highlighted by yellow arrowheads) in the DB  $\text{La}_2\text{O}_3$  ceramic are visible.  $\langle a \rangle$  and  $\langle c \rangle$  dislocation segments are highlighted by green and blue arrowheads, respectively. (D) The corresponding diffraction pattern of the DB  $\text{La}_2\text{O}_3$  in (B) and (C), indicating the observation direction of the TEM images shown in (B) and (C), respectively. (E) The neutron diffraction profiles of the present sample at different strains ( $\epsilon$ ). (F) The dislocation densities of  $\langle a \rangle$ ,  $\langle c \rangle$ , and  $\langle c + a \rangle$  dislocations in the DB  $\text{La}_2\text{O}_3$  ceramics and the dislocation densities in Mo at different engineering strains, measured by neutron diffraction in (E). The results reveal that the total dislocation density of the ductile DB  $\text{La}_2\text{O}_3$  ceramics is comparable to that of Mo metal after increasing the tensile straining to 35%, indicating that our borrowing-dislocations strategy efficiently facilitates the generation and multiplication of dislocations within ceramics, like in metals, even under room temperature and atmospheric pressure conditions.



planes and do not contribute to shear components. Therefore, the glide of  $\langle c + a \rangle$  dislocations in  $\text{La}_2\text{O}_3$  with a hexagonal structure provides additional plasticity in the crystallographic  $\langle c \rangle$  direction, thus satisfying the Von Mises plasticity criteria and enabling plastic deformation at multiple slip systems (34). Notably, the total dislocation density of the ductile DB  $\text{La}_2\text{O}_3$  ceramic ( $3.12 \times 10^{15} \text{ m}^{-2}$ ) is comparable to that of the Mo metal ( $3.85 \times 10^{15} \text{ m}^{-2}$ ) after increasing the tensile strain to 35% (Fig. 3F). Our strategy efficiently facilitates the generation and multiplication of dislocations within ceramics, even under room temperature and atmospheric pressure conditions.

To delve deeper into the underlying mechanisms governing the formation of high-density dislocations within ceramics, we conducted a comprehensive analysis of the dislocation motion on the tailored orderly-bonded interface under tensile loading. Crucially, we found that the orderly-bonded interface can effectively transfer bundles of dislocations from the Mo metal to the  $\text{La}_2\text{O}_3$  ceramic during tensile deformation (Fig. 4A and movie S4). Specifically, upon initial loading, we observed bundles of dislocations within the Mo metal, subsequently migrating toward the metal-ceramic interface. Instead of accumulating at the heterointerface (35, 36), these dislocation bundles were found to transfer into the ceramic and continued to propagate into its interior. Afterward, more bundles of dislocations in the metal were continuously generated and then effectively transferred into the ceramic through the tailored orderly-bonded interface. This process endows the ceramic with excellent tensile ductility. Meanwhile, it offers a comprehensive explanation for the varying slopes in the elastic reloading curve (Fig. 2A). Namely, in the engineering stress-strain curve of the DB  $\text{La}_2\text{O}_3$  sample (Fig. 2A), the initial slope during elastic reloading corresponds to that of the elastic region for pure metal (fig. S13), followed by a transition to the slope characteristic of normal ceramic behavior, reflecting the respective dislocation motions within each substance. Thus, the observed variations in the slopes of the serrations for DB  $\text{La}_2\text{O}_3$  serve as compelling evidence that the enhanced tensile ductility is a result of our borrowing-dislocations strategy rather than direct dislocation nucleation within the ceramic.

Accordingly, we focused on a localized metal-ceramic interface in an in situ tensile sample after several deformations to further understand the effect of the interface on the borrowing-dislocations process from metal to ceramic (Fig. 4B and movies S5 and S6). Initially, we observed dislocations predominantly in the metal. With increasing tensile strain, a discernible number of metal-inherited dislocations slipped toward the interface. Notably,

only within a brief period of time, these dislocations slipped into the ceramic through the orderly-bonded interface, despite few metal dislocations near the interface. This observation substantially deviates from previous findings, which posited that a high density of dislocations is required to trigger the ceramic dislocation initiation, a phenomenon typically obtained in nanoscale compressive plasticity (37). For the reference  $\text{La}_2\text{O}_3$ -Mo sample, without the benefit of interfacial mediation, metal dislocations were found to accumulate at the heterointerface. We observed a limited number of dislocations within the ceramic, and no discernible multiplication of these dislocations was evident. Finally, the large stress concentration caused by the dislocation accumulation led to interfacial cracking (fig. S14). The

fracture failure of the reference  $\text{La}_2\text{O}_3$ -Mo differs markedly from that of the ductile DB  $\text{La}_2\text{O}_3$  ceramic (Fig. 2B and fig. S7). These results directly demonstrate that the orderly-bonded interface, acting as a dislocation transfer channel, facilitates the continuous transfer of dislocation bundles from metal to ceramic rather than blocking the dislocations as normally observed (38). In addition, an in situ bending test under TEM reaffirms that the DB  $\text{La}_2\text{O}_3$  ceramic featuring the tailored orderly-bonded interface displays an abnormally high resistance to bending fracture, enduring angles of up to  $90^\circ$  without the initiation of microcracks (Fig. 4C). Similarly, the orderly-bonded interface can easily transfer dislocation bundles from Mo metal to  $\text{La}_2\text{O}_3$  ceramic during bending deformation (Fig. 4D and movies S7

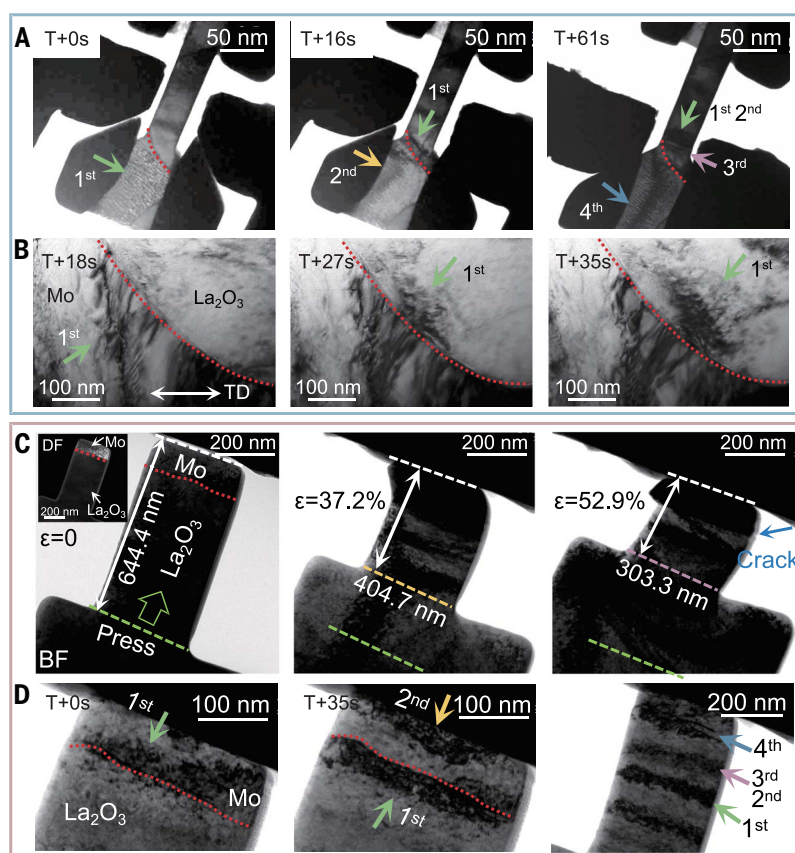
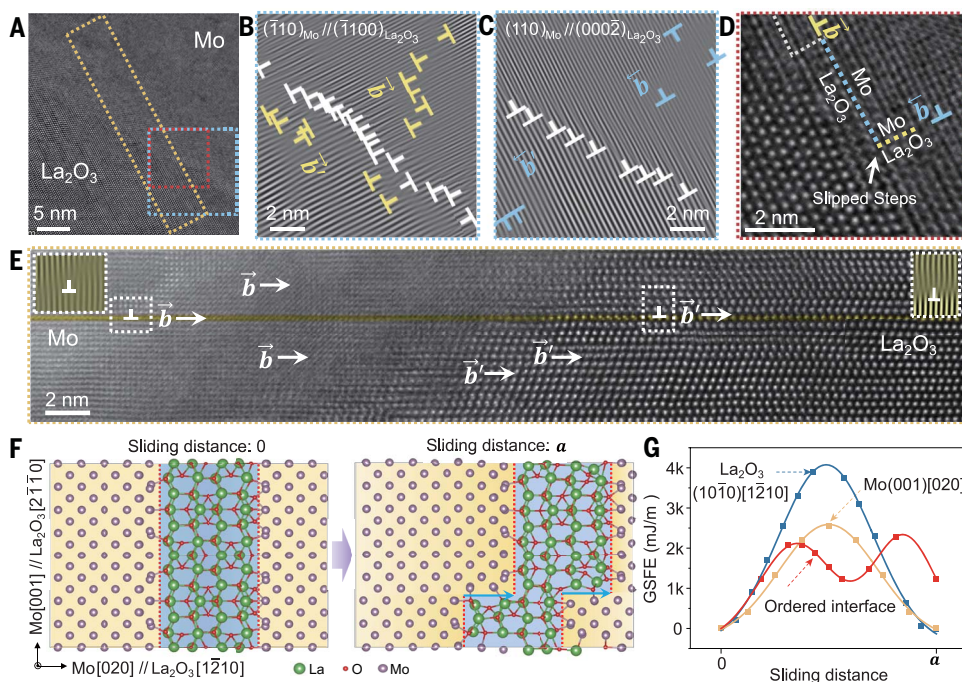


**Fig. 4. In situ tensile and bending tests of the DB  $\text{La}_2\text{O}_3$  sample under TEM.** (A) Snapshot images from the real-time movies (movie S4) of in situ tensile test on the DB  $\text{La}_2\text{O}_3$  sample captured at different times. (B) More detailed information on the dislocation transference at the orderly-bonded interface under tensile deformation, showing that the present tailored metal-ceramic interface realized the dislocation transference from metal to ceramic, thus demonstrating that our borrowing-dislocation strategy successfully conferred the exceptional tensile ductility to ceramics as shown in (A). (C and D) Snapshot images from the real-time movies (movies S7 and S8) of the in situ bending test on the DB  $\text{La}_2\text{O}_3$  sample captured at different times, displaying abnormally high resistance to bending fracture, enduring angles of up to  $90^\circ$  without the initiation of microcracks. (D) More detailed information on the dislocation transference at the orderly-bonded interface under compression stress, showing that the orderly-bonded interface can easily transfer dislocation bundles from Mo metal to  $\text{La}_2\text{O}_3$  ceramic during bending deformation. This process endows the ceramic with excellent bending plasticity, encompassing both compressive and tensile plasticity. The red dotted lines indicate the orderly-bonded interface. The colored arrowheads indicate sequentially occurring dislocation bundles.



**Fig. 5. The proposed dislocation mechanism.**

(A) HAADF-STEM image of the tailored orderly-bonded interface with several dislocations after tensile deformation. (B to E) The magnified views of the dashed boxes in (A). Specifically, (B) and (C) are IFFT images selected by different conditions on the basis of the criteria that the planes between Mo and  $\text{La}_2\text{O}_3$  are parallel, showing one possible mechanism of the dislocation transformation from metal to ceramic. (D) A typical example of a slipped step was found at the orderly-bonded interface. (E) A localized HAADF-STEM image selected from (A) shows that the slip planes of the dislocation in Mo and  $\text{La}_2\text{O}_3$  were located on the same crystallographic plane. (F) Interface model of  $\text{Mo}[001]//\text{La}_2\text{O}_3[2\bar{1}\bar{1}0]$  and  $\text{Mo}(020)//\text{La}_2\text{O}_3(0\bar{1}10)$  as depicted Fig. 1D, based on the experimental observations. (G) The calculated GSFE across the interface from Mo to  $\text{La}_2\text{O}_3$ , through partial slip along  $\text{Mo}(001)[020]$  and  $\text{La}_2\text{O}_3(10\bar{1}0)[12\bar{1}0]$  directions by one interplanar spacing ( $a$ ) of  $\text{La}_2\text{O}_3(0001)$ , as depicted in (F). The resulting landscape reveals a bimodal characteristic, with a maximum GSFE of  $2288.5 \text{ mJ/m}^2$ , which is comparable to that in bulk Mo ( $2543.9 \text{ mJ/m}^2$ ) but substantially lower than that in  $\text{La}_2\text{O}_3$  ( $3897.1 \text{ mJ/m}^2$ ). This reduction suggests that the nucleation and stepwise glide of the partial dislocations across the ordered interface are energetically favorable compared with that within the bulk ceramic.



and S8). This process endows the ceramic with excellent bending plasticity, encompassing both compressive and tensile plasticity. Furthermore, we found that the borrowed dislocations exhibit a capacity for continuous slippage and multiplication within the ceramic subsequent to their transference across the metal-ceramic interface, and then these ceramic dislocations could continuously slip across the ceramic-ceramic interfaces during tensile deformation (fig. S15 and movie S9).

We investigated the process of dislocation movement from the metal to ceramic using HAADF-STEM combined with inverse fast Fourier transform (IFFT) analysis (Fig. 5 and fig. S16). Initially, as shown in the undeformed sample, the metal-ceramic interface was nearly straight, characterized by a sharp demarcation of the interface between metal and ceramic (fig. S16A). After tensile deformation, we observed a distinct metal-ceramic interface with several dislocations (Fig. 5A). Interestingly, the previously linear interface in the undeformed sample became curved, and the demarcation between the metal and ceramic interface became indistinct (fig. S16B), which indicates a deformation compatibility between the metal and ceramic during the tensile deformation.

To further understand the underlying mechanism governing deformation compatibility at the interface between the metal and ceramic, we focused on a magnified view of the deformed metal-ceramic interface (Fig. 5A) with specific

lattice plane coordination using IFFT analysis (Fig. 5, B and C). First, we directed our attention toward the alignment of the  $(\bar{1}10)$  planes of Mo with the  $(\bar{1}100)$  planes of  $\text{La}_2\text{O}_3$  (Fig. 5B). We observed a substantial presence of edge dislocations on both sides of the interface. Moreover, these edge dislocations shared parallel slip directions, indicating their potential to slip through the interface along the direction perpendicular to the continuous planes, thus transferring from the metal side into the ceramic side. We found a similar phenomenon when the  $(110)$  planes of Mo were parallel to the  $(000\bar{2})$  planes of  $\text{La}_2\text{O}_3$  (Fig. 5C). Additionally, we can see that the slip planes of the dislocations within Mo and  $\text{La}_2\text{O}_3$  coincided on the same crystallographic plane (Fig. 5E), thus providing direct evidence for the transmission of dislocations across the orderly-bonded interface. Consequently, the presence of the slipped step at the metal-ceramic interface (Fig. 5D) coupled with the one captured under the tensile loading (fig. S17) leads to the shape change of the interface, which we believe could be reasonably attributed to the dislocation motions (39, 40).

We investigated the detailed dislocation transformation at the tailored orderly-bonded interface by first-principles calculations, aiming to provide a possible formation mechanism of the slipped steps we observed (Fig. 5D). To simplify the model, we treated the formation of slipped steps as stacking faults

across the ordered  $\text{La}_2\text{O}_3$ -Mo interface (Fig. 5F). Accordingly, we calculated the generalized stacking fault energy (GSFE), a parameter reflecting resistance to dislocation nucleation and glide. We constructed an identical interface model of  $\text{Mo}[001]//\text{La}_2\text{O}_3[2\bar{1}\bar{1}0]$  and  $\text{Mo}(020)//\text{La}_2\text{O}_3(0\bar{1}10)$  as illustrated in Fig. 1D. Then, we considered the partial slip along the  $\text{Mo}(001)[020]$  and  $\text{La}_2\text{O}_3(10\bar{1}0)[12\bar{1}0]$  directions by one interplanar spacing ( $a$ ) of  $\text{La}_2\text{O}_3(0001)$  oriented along the continuous planes (Fig. 5F). The resulting landscape reveals a bimodal characteristic, with a maximum GSFE of  $2288.5 \text{ mJ/m}^2$  in the DB  $\text{La}_2\text{O}_3$  upon transferring the orderly-bonded interface (Fig. 5G). We then compared this GSFE with those of the same slip systems in bulk materials along the  $\text{La}_2\text{O}_3(10\bar{1}0)[12\bar{1}0]$  and  $\text{Mo}(001)[020]$  directions, respectively, allowing a direct comparison of the GSFE in different materials (Fig. 5G). The result shows that the GSFE in DB  $\text{La}_2\text{O}_3$  is comparable to that in bulk Mo ( $2543.9 \text{ mJ/m}^2$ ) but substantially lower than that in bulk  $\text{La}_2\text{O}_3$  ( $3897.1 \text{ mJ/m}^2$ ). This reduction suggests that the nucleation and stepwise glide of partial dislocations across the ordered interface are energetically favorable compared with that in the bulk ceramic. Consequently, it facilitates dislocation transfer from metals to ceramics and provides compelling evidence for the feasibility of dislocation transfer across the orderly-bonded interface. Furthermore,  $\text{La}_2\text{O}_3$ , as an ionic-type oxide, undergoes intricate processes

of dislocation movement and multiplication that will require additional observations to fully unravel.

Despite  $\text{La}_2\text{O}_3$  being a ceramic material with a hexagonal crystal structure, traditionally lacking ductility at room temperature, the borrowing-dislocations strategy enables  $\text{La}_2\text{O}_3$  ceramics to have improved tensile ductility by borrowing extensive metal-assisted dislocation bundles. Further, we have extended this strategy to other ceramic-metal systems, such as  $\text{CeO}_2\text{-Mo}$ . In the  $\text{CeO}_2$  with a fluorite structure, we also observed extensive dislocations and, consequently, good tensile ductility (figs. S18 to S20).

## REFERENCES AND NOTES

1. R. Riedel *et al.*, *Nature* **382**, 796–798 (1996).
2. T. Ohji, M. Singh, Eds., *Engineered Ceramics: Current Status and Future Prospects* (Wiley, 2016).
3. R. N. Katz, *Science* **208**, 841–847 (1980).
4. F. Bouville *et al.*, *Nat. Mater.* **13**, 508–514 (2014).
5. J. Li *et al.*, *Nat. Mater.* **19**, 999–1005 (2020).
6. Z. Shen, Z. Zhao, H. Peng, M. Nygren, *Nature* **417**, 266–269 (2002).
7. P. Baldus, M. Jansen, D. Sporn, *Science* **285**, 699–703 (1999).
8. Y. Wu *et al.*, *Nature* **626**, 779–784 (2024).
9. J. Karch, R. Birringer, H. Gleiter, *Nature* **330**, 556–558 (1987).
10. C. Jia *et al.*, *Nat. Commun.* **11**, 3732 (2020).
11. J. Li *et al.*, *Sci. Adv.* **5**, eaaw5519 (2019).
12. Y. Yue *et al.*, *Nature* **582**, 370–374 (2020).
13. Q. Huang *et al.*, *Nature* **510**, 250–253 (2014).
14. L. Porz *et al.*, *Mater. Horiz.* **8**, 1528–1537 (2021).
15. Y. Han *et al.*, *Nat. Commun.* **13**, 2871 (2022).
16. D. Hull, D. J. Bacon, *Introduction to Dislocations* (Elsevier, ed. 5, 2011).
17. F. R. Nabarro, M. S. Duesbery, *Dislocations in Solids*, **vol. 11** (Elsevier, 2002).
18. X. Li, Y. Wei, L. Lu, K. Lu, H. Gao, *Nature* **464**, 877–880 (2010).
19. B. R. Lawn, N. P. Padture, H. Cai, F. Guiberteau, *Science* **263**, 1114–1116 (1994).
20. J. Zhang *et al.*, *Science* **378**, 371–376 (2022).
21. T. R. Wei *et al.*, *Science* **369**, 542–545 (2020).
22. E. J. Frankberg *et al.*, *Science* **366**, 864–869 (2019).
23. X. Shi *et al.*, *Nat. Mater.* **17**, 421–426 (2018).
24. U. W. Pohl, *Epitaxy of Semiconductors: Physics and Fabrication of Heterostructures* (Springer, ed. 2, 2020).
25. Y. Sun *et al.*, *Nat. Photonics* **10**, 595–599 (2016).
26. Y. Cui *et al.*, *Science* **383**, 212–219 (2024).
27. Materials and methods are available as supplementary materials.
28. C. R. Massey *et al.*, *Acta Mater.* **200**, 922–931 (2020).
29. X. Yan *et al.*, *Nat. Commun.* **14**, 2788 (2023).
30. Y. Z. Li, M. X. Huang, *J. Mech. Phys. Solids* **121**, 313–327 (2018).
31. M. A. Lebyodkin, Y. Brechet, Y. Estrin, L. P. Kubin, *Phys. Rev. Lett.* **74**, 4758–4761 (1995).
32. L. Zhang *et al.*, *Phys. Rev. Lett.* **125**, 055501 (2020).
33. M. S. Ding *et al.*, *Nano Lett.* **16**, 4118–4124 (2016).
34. C. Bettles, M. Barnett, Eds., *Advances in Wrought Magnesium Alloys: Fundamentals of Processing, Properties and Applications* (Woodhead Publishing, 2012).
35. Z. Lei *et al.*, *Nature* **563**, 546–550 (2018).
36. T. J. Jang *et al.*, *Nat. Commun.* **12**, 4703 (2021).
37. J. Zou *et al.*, *J. Mater. Sci. Technol.* **134**, 89–94 (2023).
38. J. Wang, A. Misra, *Curr. Opin. Solid State Mater. Sci.* **18**, 19–28 (2014).
39. L. Zhong, Y. Zhang, X. Wang, T. Zhu, S. X. Mao, *Nat. Commun.* **15**, 560 (2024).
40. Q. Huang *et al.*, *Nat. Commun.* **12**, 6695 (2021).

## ACKNOWLEDGMENTS

We acknowledge L. H. He, J. Chen, and S. H. Deng for assistance with the neutron powder diffraction experiments, which were performed at the general purpose powder diffractometer of the China Spallation Neutron Source (CSNS), Dongguan, China; Z. Y. Yu and X. Y. Ye (Fuzhou University) and F.Y.F. Chan (The University of Hong Kong) for assistance with TEM characterization; and

Y. Z. Chen (Northwestern Polytechnical University) and X. D. Han (Beijing University of Technology) for fruitful discussions about our work. **Funding:** J.S.W. acknowledges financial support from the National Natural Science Foundation of China (grant 52130407) and the National Key Research and Development of China (grant 2022YFB3705402). M.X.H. acknowledges support from the National Key Research and Development Program of China (grant 2019YFA0209900), the National Natural Science Foundation of China (grant U1764252), the Research Grants Council of Hong Kong (grant 17307123), and the New Cornerstone Science Foundation through the XPLOER PRIZE. J.Z. acknowledges support from the Young Elite Scientists Sponsorship Program by China Association for Science and Technology (CAST) (grant 2024QNRC001). **Author contributions:** J.S.W., K.X.C., and M.X.H. supervised the research. K.X.C. conceived of the idea and designed the experiments. L.R.D. and J.Z. designed and fabricated the specimens. L.R.D. and J.Z. worked on the in situ TEM and TEM characterization. Y.X.G. worked on the DFT calculations. M.W. and Y.Z.L. conducted the neutron diffraction characterization. L.R.D., J.Z., Y.Z.L., and K.X.C. wrote the manuscript. All authors discussed the results and commented on the manuscript. **Competing interests:** The authors declare that they have no competing interests. **Data and materials availability:** All data are available in the manuscript or the supplementary materials. **License information:** Copyright © 2024 the authors, some rights reserved; exclusive licensee American Association for the Advancement of Science. No claim to original US government works. <https://www.science.org/about/science-licenses-journal-article-reuse>

## SUPPLEMENTARY MATERIALS

[science.org/doi/10.1126/science.adp0559](https://doi.org/10.1126/science.adp0559)  
Materials and Methods  
Supplementary Text  
Figs. S1 to S20  
Tables S1 to S3  
References (41–50)  
Movies S1 to S9

Submitted 11 March 2024; accepted 4 June 2024  
10.1126/science.adp0559